2025, 10(3) e-ISSN: 2468-4376

https://www.jisem-journal.com/

**Research Article** 

# A Study on the Relationship Between the Microstructure, Tensile Stress, and I-Section Width in Thin-Walled Spheroidal Graphite Iron Connecting Rods

Vaibhav Maniar<sup>1\*</sup>, Pinank Patel<sup>2</sup>

<sup>1\*</sup>Research Scholar in Department of Mechanical Engineering, Marwadi University, Rajkot-Morbi Road, Rajkot 360 003 Gujarat, India E-mail: vrmaniar@gmail.com

<sup>2</sup>Associate Professor in Department of Mechanical Engineering, Marwadi University, Rajkot-Morbi Road, Rajkot 360 003 Gujarat, India E-mail: Pinank.patel@marwadieducation.edu.in

#### ARTICLE INFO

### ABSTRACT

Received: 20 Nov 2024 Revised: 27 Dec 2024

-

Accepted: 12 Jan 2025

Automotive components must be lighter to reduce fuel consumption. Component production must prioritize energy efficiency and environmental sustainability. Aluminium is characterized by its lightweight properties; however, its production is energy intensive. Spheroidal graphite iron provides significant design flexibility, and the use of thin wall casting can reduce its weight, enabling competition with less weight components. The development of a 2 mm I-section width connecting rod that satisfies previous research criteria has prompted further exploration into the reduction of I-section width. These boosts connecting rod weight reduction. This effort seeks to achieve repeatability in 2 mm I-section width design and capability to generate 1.5 mm I-section width via casting design. Thin wall casting solidification rates are important owing to product widths. It also examines I-section width and tensile stress. Foundry size I-sections were 2 mm and 1.5 mm thick. The microstructure and tensile load of all I-sections were characterized. Tensile testing assessed tensile load. Microstructure observations indicated that the I-section microstructure differs from that of the big end microstructure, except for unique casting location. Meanwhile, the tensile load demonstrated comparable mean tensile load between 2 mm and 1.5 mm, aligning with the requirements for connecting rod tensile loads. This work created casting models for making equivalent-load thin wall spheroidal graphite iron (TWSG) connecting rods.

**Keywords:** Microstructure, spheroidal graphite iron, simulation, I section, connecting rod, tensile test.

### 1. Introduction

Modern car components are lightweight to minimize energy consumption. Lighter components should meet design requirements like the originals. Low production energy, consumer, and environmental friendliness are also important [1]. When considering weight reduction, many choose for aluminium as an alternative material. Unfortunately, metal lacks energy efficiency and environmental friendliness. Primary aluminium manufacturing requires three times more energy than primary iron.[2] An investigation analysed the impact of replacing engine block materials on weight reduction. This investigation assessed energy intensity and emissions associated with aluminium and cast-iron engine blocks. Tail-pipe emissions are not a reliable metric for assessing lightweight and fuel-saving strategies.[3]

Weight reduction via engine block material substitution was examined. The study analysed energy requirement and emissions associated with aluminium and Grey CI engine blocks. Tailpipe emissions are insufficient for assessing lightweight and fuel-saving strategies. The utilization of composite structures is influenced by the compromise between lightweight performance and manufacturing prices [4, 5]. Thin wall casting process reduces spheroidal graphite iron weight and meets energy efficiency and emission requirements. Martinez helped to reduce mass of connecting rod by 33% using this method. The use of Martinez made it possible to produce thin wall casting for automobile parts [6-8].

2025, 10(3) e-ISSN: 2468-4376

https://www.jisem-journal.com/

### **Research Article**

For weight reduction, thin wall casting method reduces component width in sections or full areas. This may alter mechanical characteristics. While substitutes must meet design standards.[9, 10]. As previously stated, lowering component width should not affect mechanical qualities. A change in mechanical qualities may disrupt mechanical properties [11, 12]. Nickel inclusion of 0.87 wt% reduces cementite production and enhances spheroidal graphite iron [13]. Enhanced carbon equivalent (CE) values result in enhanced hardness, ultimate tensile strength, and wear strength, but decreased in % elongation. With the same proportion of Carbon equivalent values, increasing casting width decreases hardness, ultimate tensile strength, and yield strength while increasing elongation.[14] In addition to discovered that , when pearlite and nodule count waning, Ultimate tensile strength and yield strength waning. Flexural strength increase as ultimate tensile strength and yield strength decrease.[15]. It was said that thin wall spheroidal graphite iron may reduce mass like aluminium while improving mechanical qualities. Use three light-weight cases: a separate engine block casing and cast iron component replacement.[10, 16].

This investigation seeks to examine the effects of different I-section widths (specifically 2 mm and 1.5 mm) on metallography, tensile strength and percentage elongation. This research delves deeper into the reproducibility of the casting design used to make the connecting rods.

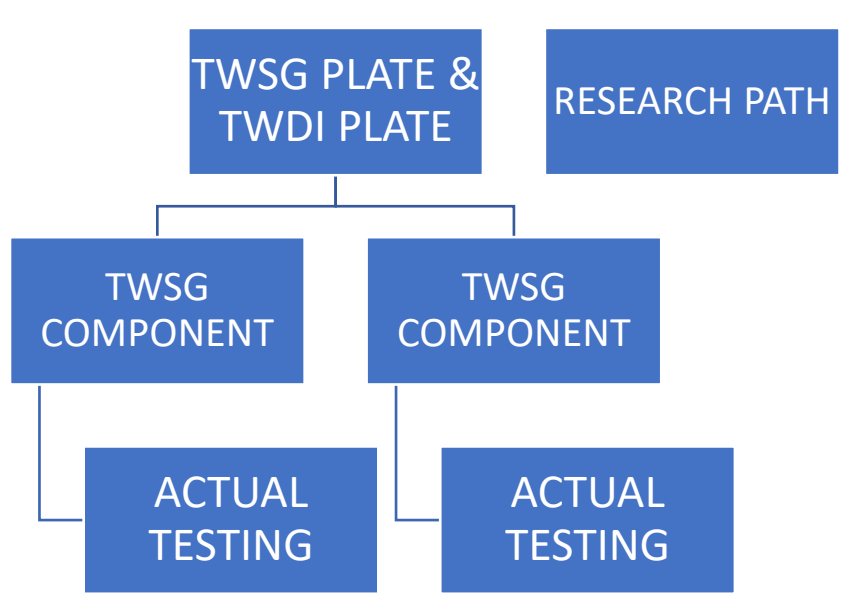


Figure 1 Research path

This effort is a component of an ongoing research sequence, as seen in Figure 1, which underway for creation of TWSG lamina to ascertain the casting shape and characterisation. Subsequently, the casting strategy is used to manufacture TWSG automobile parts. All the study is conducted within an industry context [17].

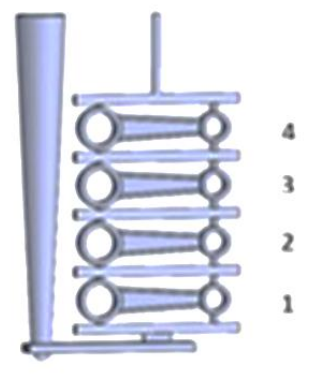


Figure 2 Casting design

This design is an evolution of the TWDI plates casting design with the identification numbers Poo201600907,IDP000039503 [17], IDP00040306 [18], The process involves vertical casting, which produces four connecting rods per mold.

2025, 10(3)

e-ISSN: 2468-4376

https://www.jisem-journal.com/

### **Research Article**

Fig.3 depicts the dimensions of the connecting rod. At Fine Cast Casting produced two connecting rod styles. Connecting rods having width of I-section, 2 mm and another one was having width of I-section was 1.5 mm. The sample count was sixteen.

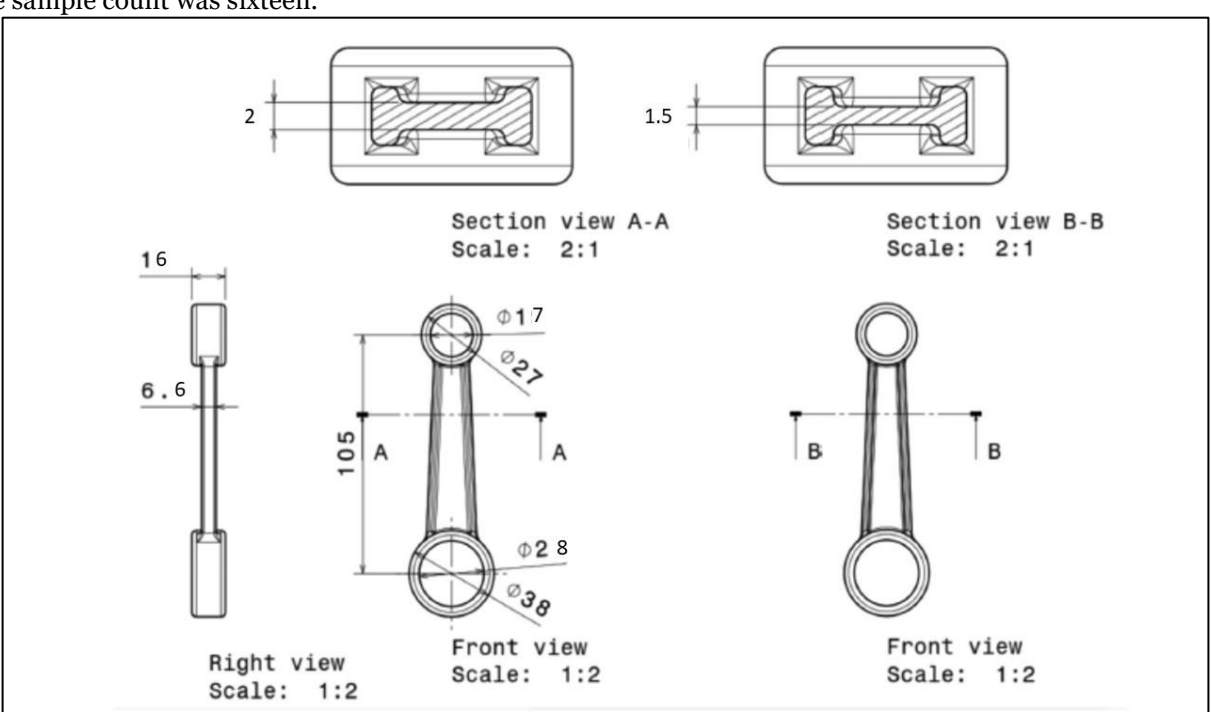


Figure 3 Connecting rod design

All connecting rods were made using EN-GJS-450-10 commercial liquid metals from three pouring groups. This form was used to verify casting design repeatability. First group, B1, produced 3 mm I-section-thick connecting rods. Eight connecting rods were made. The second group, B2, produced 2 mm and 1.5-mm I-sections. Four 2 mm and four 1.5 mm connecting rods were made. Group 3 (B3) has the same specifications as group 2. Eight samples were taken for 2 mm and 1.5 mm I-section connecting rods.

Pouring temperatures ranged from 1400 to 1435 °C, with a 6-8 s pouring period per mold. This investigation employed tapping and pouring temperatures based on commercial items. Sandblasting was used to clean the casting after 4-5 hours. Fatling process was carried out afterwards. This study used a 1000-kilogram induction furnace to make liquid metal. Materials used for charging include foundry return, steel scrap, ferrosilicon, ferromanganese. The pouring temperatures were 1435, 1420, and 1405 °C. Different pouring temperatures exist, but all are above the foundry norms. Table 1 lists and codes each connecting rod. The macro chemistry of each group poured is presented in Table 2.

Table 1 Connecting rod coding

Those Teorniconing Fourtoning								
Pouring Group	Width	Sample code	Pouring Group	Width	Sample code			
B1	3	1	B2	2	P			
		2			Q			
		3			R			
		4			S			
		5	В3	1.5	T			
		6			U			
		7			V			
		8			W			

Table 2 Chemical makeup

Tuote = enemieur muneup								
Element	Standard (wt.%)		Results of the testing (wt.%)					
	EU	Foundry	B1	B2	В3			
C	3.30-3.50	3.50-4.0	3.63	3.72	3.88			
Mn	0.10-0.30	0.30-0.60	0.3	0.35	0.41			

2025, 10(3)

e-ISSN: 2468-4376

https://www.jisem-journal.com/

### **Research Article**

S	Max. 0.020	Max. 0.020	0.026	0.025	0.010
Si	3.20-3.50	2.20-2.90	1.9	2.44	2.86
P	Max. 0.300	Max. 0.020	0.020	0.01	0.021
Cr	0.03-0.08	0.04-0.08	0.04	0.06	0.08
Ni	0.05-2.00	0.5 -2	0.67	1.1	1.9
Mo	0.01-1.0	0.02-0.9	0.04	0.02	0.08
CE (%) (Calculation %C + 0.30%Si)			4.20	4.45	4.73

The liquid metal's chemical composition was analysed by using spectrometer. All the group's connecting rods were subjected to a universal testing machine to carry out the test under tensile load by using the UTEST 600 kN maximum load capacity Servo Controlled Hydraulic Universal Testing Machine, which features Double Testing Space. The test was conducted directly on the rod utilizing the fixture illustrated in Figure 4. Following tensile testing, tensile testing was conducted with the load direction reversed. Tensile rate was 0.25 mm/sec. Data included tensile load and produced deflection. The tensile test was followed by metallographic inspection of each I-section cross-section. Metallographic samples from the big end and I section are displayed in Fig. 5. After cutting and mounting, each sample's surface was magnified six times.

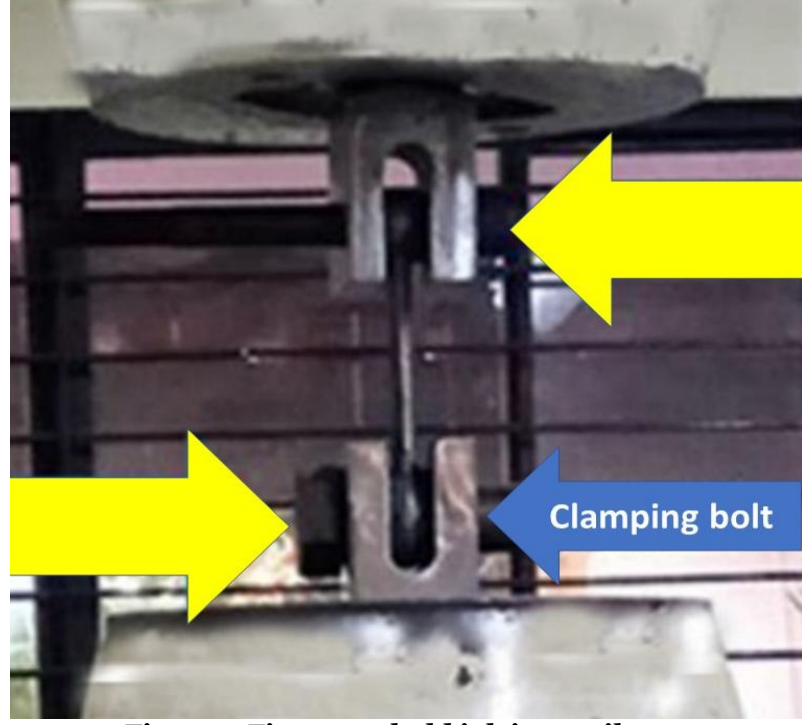


Figure 4 Fixture to hold job in tensile test



Figure 5 Placement for the metallography analysis

2025, 10(3) e-ISSN: 2468-4376

https://www.jisem-journal.com/

**Research Article** 





Figure 6 B1 batch connecting rods





(1) B1 2 MM

(2) B1 1.5 MM

Figure 7 B2 batch connecting rods





(1) B3 -2 mm

(2) B3 -1.5 mm

Figure 8 B3 batch connecting rods

2025, 10(3)

e-ISSN: 2468-4376

https://www.jisem-journal.com/

**Research Article** 

### 2. Result and discussion

Figure 6 shows that B1 connecting rods do not have casting faults. Figure 7 and 8 show that B2 and B3 do not get the same outcome. Shrinkage occurred in all 1.5-mm I-sections but not in 2 mm ones. An investigation revealed that the actions of the foundryman in charge disrupted the flow of molten liquid metal into the mold during the pouring process. This shrinkage defect was taken care by using exothermic compound into the riser location after pouring of molten metal into the mold.

The foundry standard makes no mention of molybdenum's limitations. Although molybdenum has a great affinity for carbon, it is a ferrite stabilizer. If the level of molybdenum exceeds 0.5%, it will have an impact on the iron [19, 20]. A molybdenum level of 0.5% will disrupt graphite form and quantity. B2 contains 0.02% molybdenum. Thus, Molybdenum will not affect iron [21].

Different findings were observed while comparing chemical composition to EU standards. As per EU standards, sulphur concentration exceeds the maximum limit, copper remains within limits, while molybdenum falls below the minimum requirement of 79%-99.99%. Except for molybdenum, carbon, chromium, and nickel need particular attention. B3 has 0.51% more carbon than allowed. B1 contains 28.5% more chromium than the EU standard allows, whereas B1, B2, and B3 have 85%, 79%, and 95.5% less nickel. Since EU is a broader standard and covers most of the foundry standard's issues, following discussion will focus on it. Nickel and molybdenum increase hardenability [22], but austempering is not done in this area, thus the benefit is not visible.

When comparing chemical compositions, B<sub>3</sub> has the most unmet needs. The batch with the greatest carbon content will have the most nodule development compared to the other two. B<sub>3</sub>, the lowest copper concentration, forms graphite. Given this, nodule graphite will not be a major increase. B<sub>2</sub> contains the most silicon and manganese. Silicon and manganese have a reversal function, therefore B<sub>2</sub> may have the same outcome as the other groups. B<sub>2</sub> has the most spheroidal ity since it contains the most magnesium.

Carbon equivalent (CE) testing results indicate all levels over 4.3. Each is a hyper-eutectic spheroidal graphite iron. Changes in CE values across groups are 1.9%-6.95%. The highest carbon equivalent is observed in B3 and lowest is observed in B2. Calculation yields 3% greater CE than spectrometry. The CE value is directly connected to carbide and principal graphite; therefore, the confirmation method will include reviewing microstructure data. Spheroidal graphite does not float owing to its CE value. [23]

See Figure 9, for metallographic specimens before preparation for examination. The study of each surface reveals unique colour patterns, as seen in Figs. 9-3 and 9-V. In Fig. 9, the I-section and big end have different colour patterns. This shows that microstructure matrix varies by sample. White indicates carbide, while grey indicates pearlite or pearlite-ferrite matrix. The cooling rate is affected by width of the casting as well as its design. Carbide cools faster than ferrite matrix.

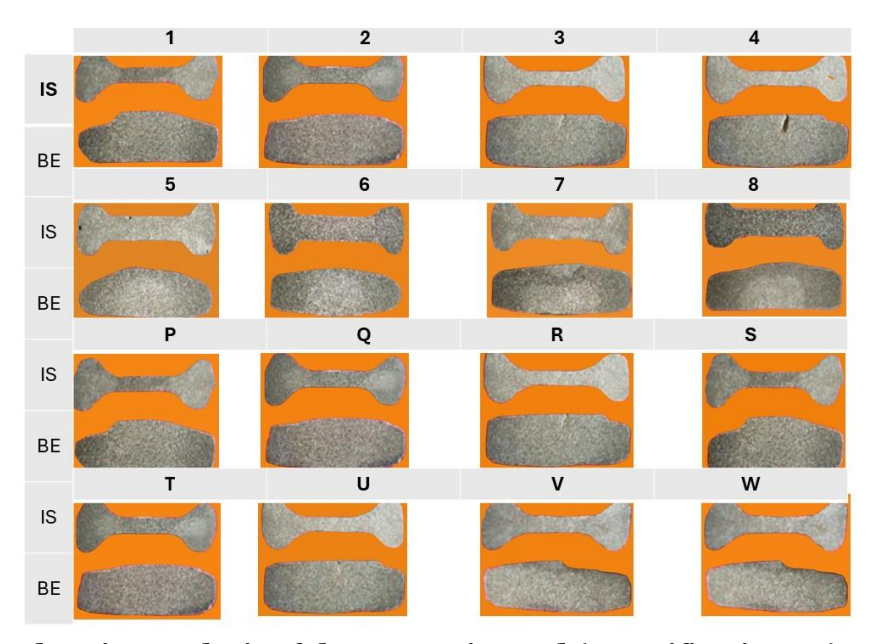


Figure 9 Comprehensive analysis of the connecting rod (Magnification-8x) IS=I Section, BE= Big End

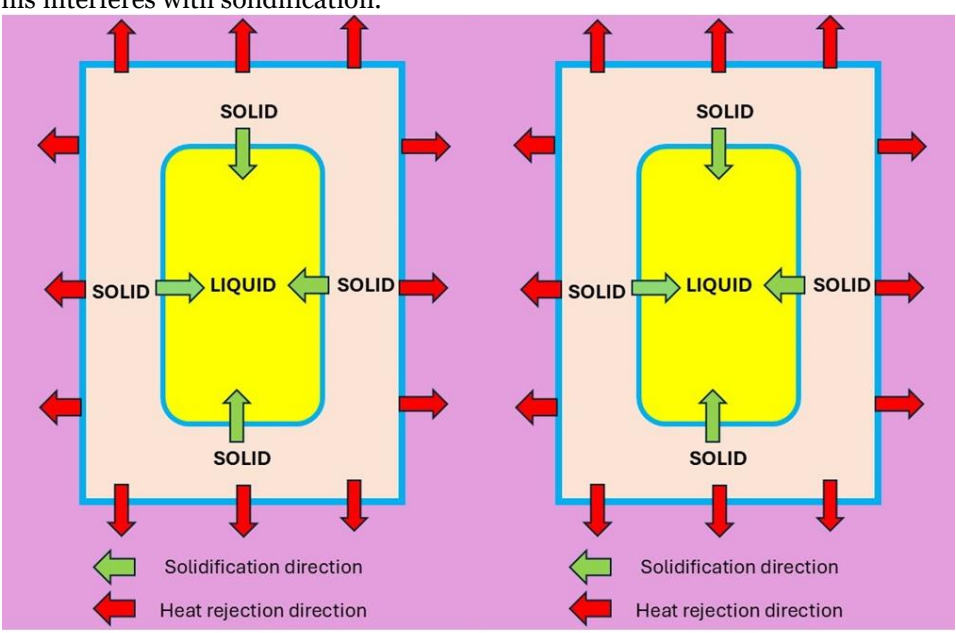
2025, 10(3)

e-ISSN: 2468-4376

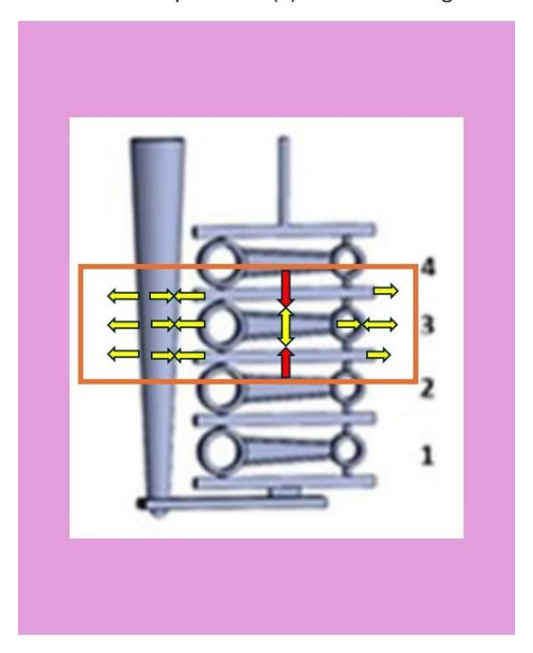
https://www.jisem-journal.com/

### **Research Article**

FIG. 10(a), [24] demonstrates the cooling process, indicating that heat (characterized by a reddish dart) dissipates from the liquid metal at every location. Site surface area and condition determine solidification rates. The solidification rate will be the same if all sites are the same size and condition. Fig. 10(b) shows the casting design's heat leaving direction schematically. This diagram indicates that heat leaving directions collide except on the right. This interferes with solidification.



(a) Schematic diagram of Solidification process (a) Schematic diagram of Solidification process



(b) Schematic diagram of heat rejection direction

2025, 10(3)

e-ISSN: 2468-4376

https://www.jisem-journal.com/

### **Research Article**

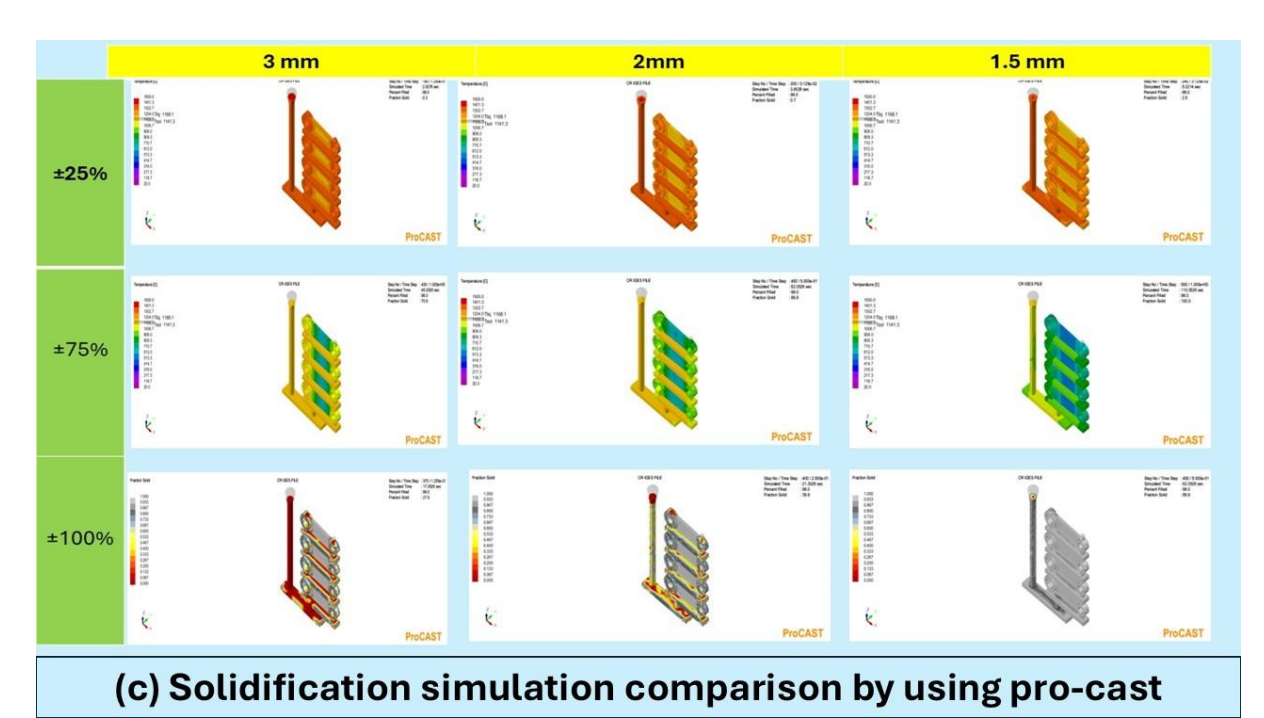
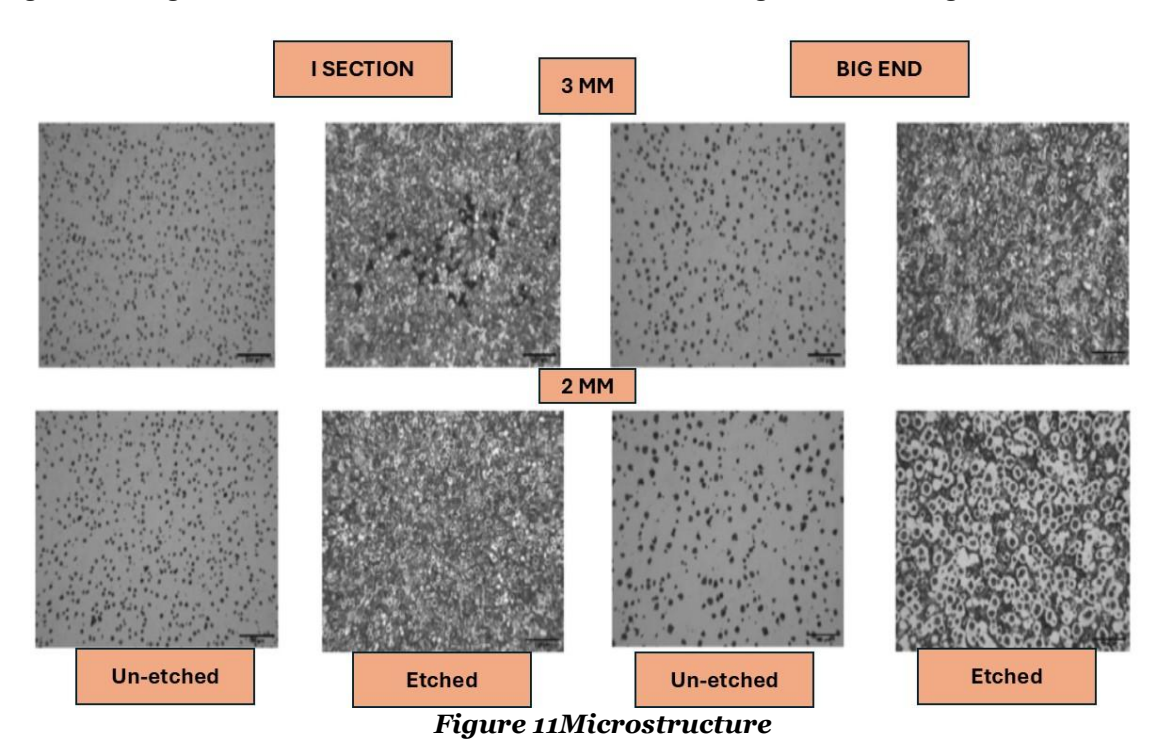


Figure 10 Effect of mold design on solidification

Figure 10(c) [25] demonstrates a simulation of solidification at three different width of I-section. The simulation reveals distinct freezing configurations corresponding to every width, with entirety freezing initiating at the centre of the I-section and progressing towards the big end. There are parallels between the schematic illustrations in Figure 10(a) and 10(b).

See Figure 11 for metallographic results. Generally, un-etched microstructures show uniform distribution of spheroidal graphite in I-section and big end areas throughout all carbon equivalent conditions. It appears that I-section has more nodules than big end. While the big end has larger nodules, I-section has smaller ones. We detected several I-section and big end problems. Figure 12 shows that I-section flaws arise during tensile testing, not casting. However, surface examination will reveal casting faults in the big end.



Copyright © 2024 by Author/s and Licensed by JISEM. This is an open access article distributed under the Creative Commons Attribution License which permitsunrestricted use, distribution, and reproduction in any medium, provided the original work is properly cited.

2025, 10(3) e-ISSN: 2468-4376

https://www.jisem-journal.com/

### **Research Article**

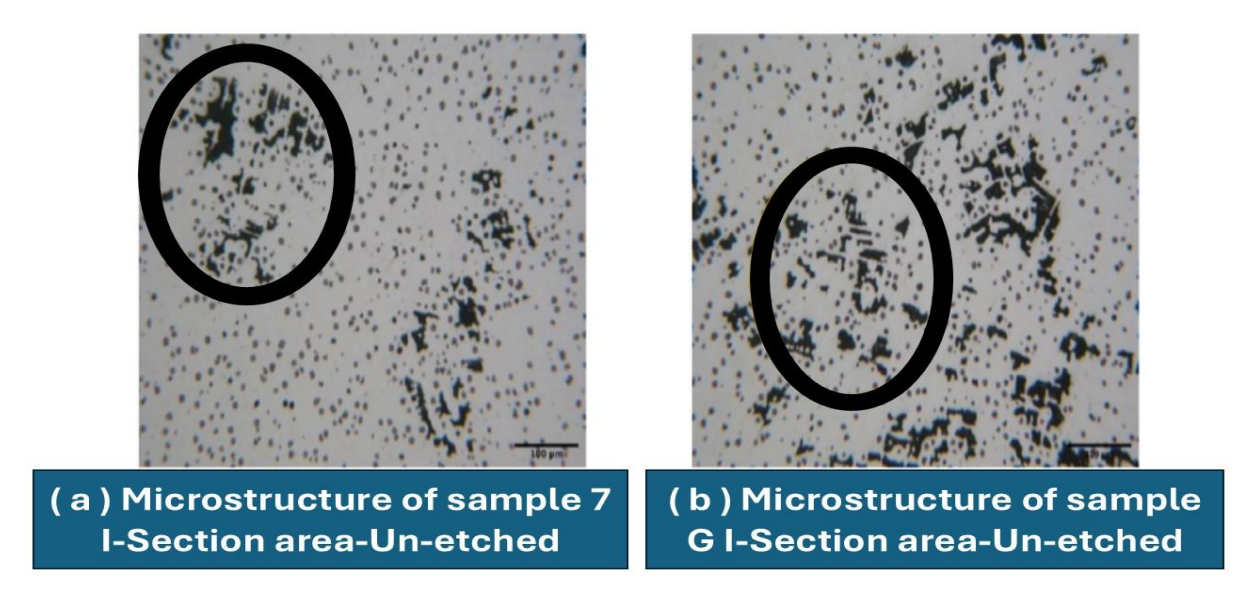


Figure 12 strain patterns following a tensile examination

Fig. 13 shows that sample W's big end has primary graphite, but un-etched connecting rod microstructures with I Section width of 2 mm have no irregularities. It's normal because this sample's CE is 4.61. Since samples 4, 5, and 7 have similar nodule sizes to the I-section and big end area, the connecting rod with a 3mm I-section width must be considered. Quantitative study will prove this. The etched microstructures show that the I-section and big end have different matrices and a mixed matrix. This confirmed the macro colour pattern analysis of each I-section and big end surface sample. The microstructure after etching revealed that carbide appears white in macro examination, while the pearlite or ferrite-pearlite matrix presents a grey appearance.

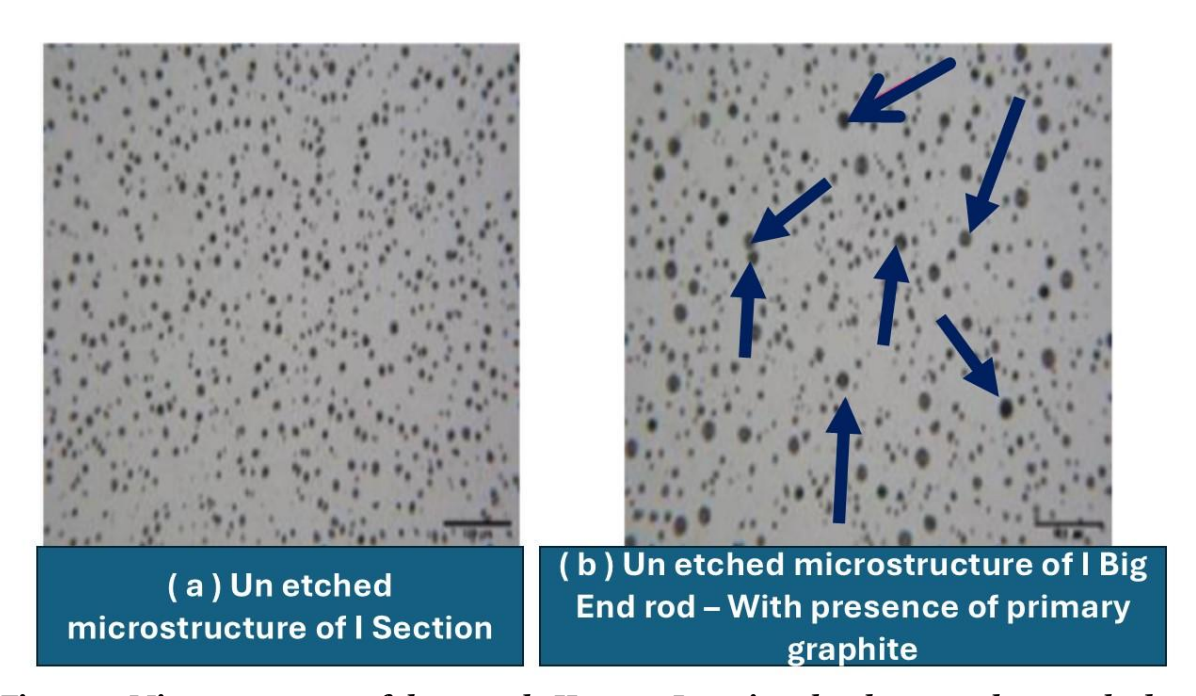


Figure 13Microstructures of the sample H-2 mm I-section that have not been etched.

Samples V and W have specialties. As seen in Figure 14, the I-section microstructure resembles the big end section. Sample V has spheroidal graphite with carbide in a ferrite matrix, while model W has it in a carbide in pearlite matrix. The CE value should explain this.

2025, 10(3) e-ISSN: 2468-4376

https://www.jisem-journal.com/

### **Research Article**

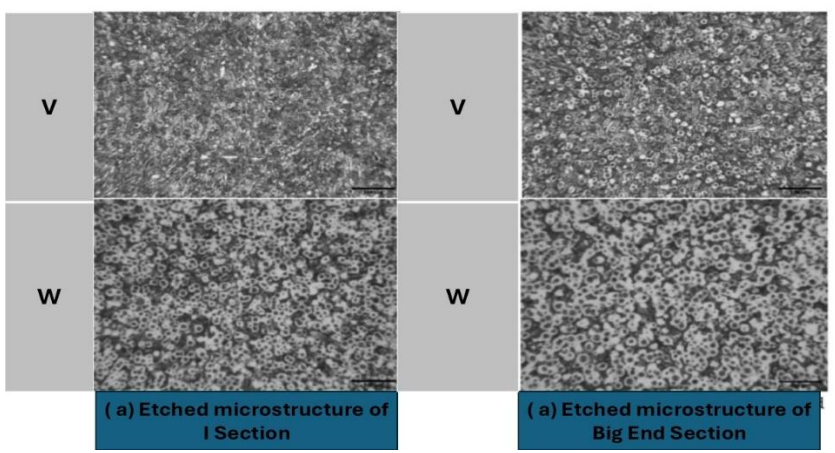


Figure 14 The microstructures of the trial W with two milimeter I-section width were etched.

Variations among the 3mm I-section and the large, oversized end are also examined. The I-section of Sample 1 contains spheroidal graphite along with ferrite embedded in a pearlite matrix, resembling its large, substantial end. Samples 3 and 4 exhibit comparable conditions yet possess distinct microstructures. **Error! Reference source not found.** illustrates two distinct microstructures in the I-section and the big end. A ferrite matrix and a ferrite-pearlite matrix consist of spheroidal graphite along with carbide.

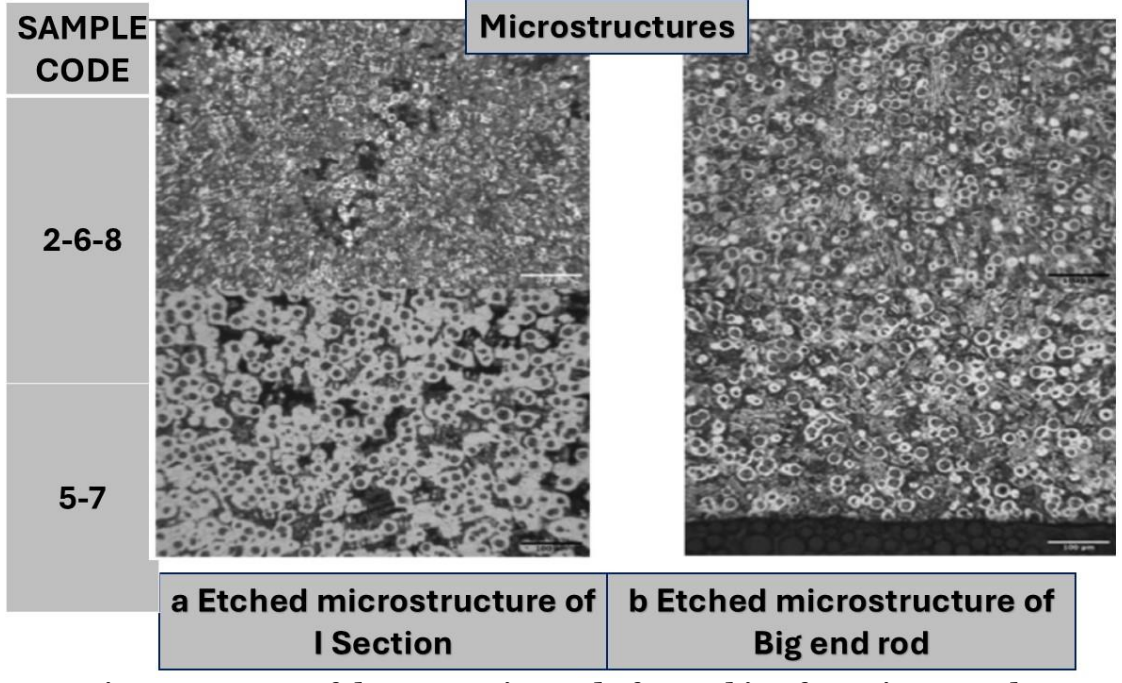


Figure 15 Microstructures of the connecting rod after etching featuring samples 2, 6, and 8 with a 3 mm I-section width, along with samples 5 and 7.

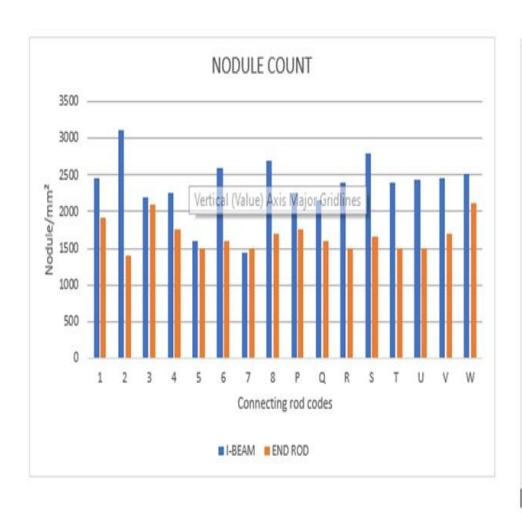
See Figure 15 for nodule count. Previously, the I-section nodule count was considered to be larger than the big end, excluding for sample 6. This is expected owing to I-section width discrepancies. I-section width was lowered while big end width was maintained to reduce connecting rod weight. In sample 7, the unetched microstructure has unusually identical spheroidal graphite sizes in the I-section and big end. Sample 5 had comparable nodule graphite size.

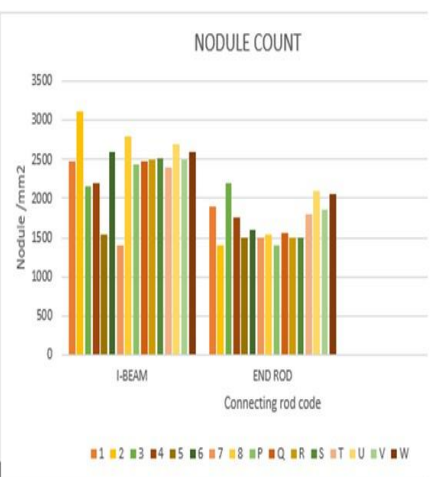
2025, 10(3)

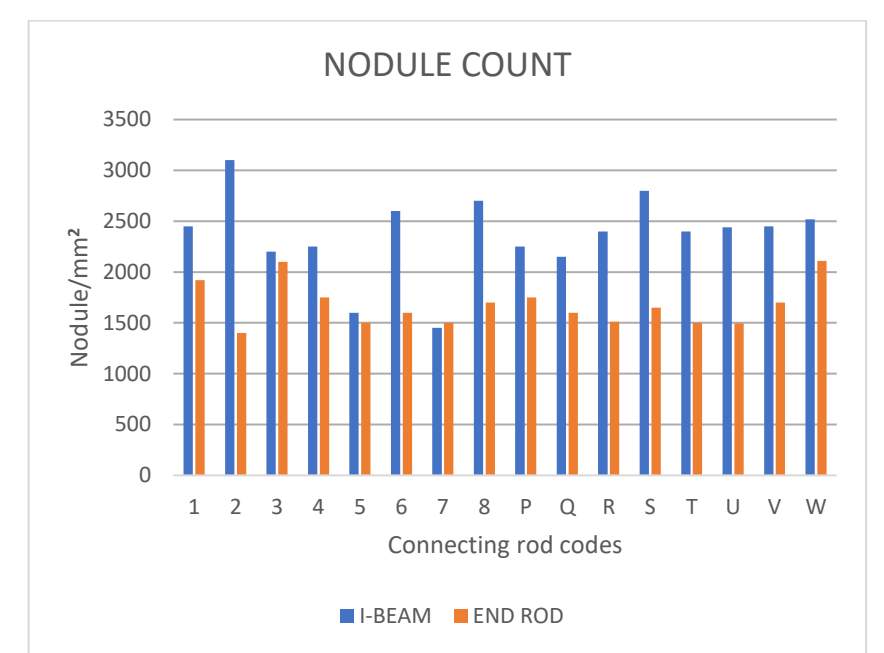
e-ISSN: 2468-4376

https://www.jisem-journal.com/

### **Research Article**







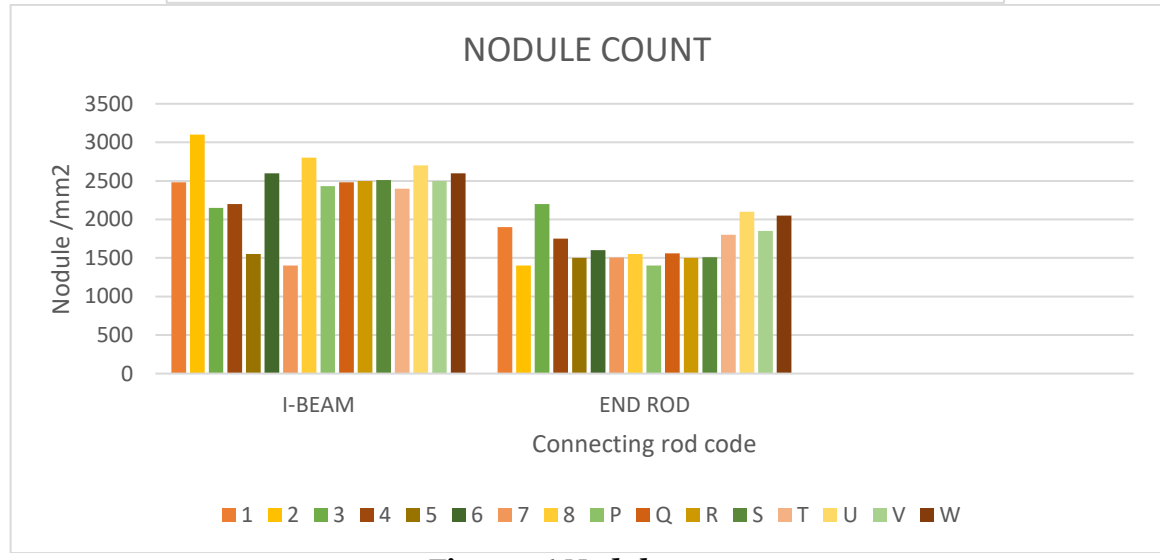


Figure 16 Nodule count

Copyright © 2024 by Author/s and Licensed by JISEM. This is an open access article distributed under the Creative Commons Attribution License which permitsunrestricted use, distribution, and reproduction in any medium, provided the original work is properly cited.

2025, 10(3) e-ISSN: 2468-4376

https://www.jisem-journal.com/

#### **Research Article**

The quantity of nodules in the 2 mm I-section ought to go beyond that in the 3 mm section due to the difference in width. The quantitative outcome was different. An inaccurate cooling rate measurement may explain this disparity.

Figure 17 illustrates the outcomes of the tensile tests performed on the connecting rods featuring I-section width of three mm and two mm. The dataset includes tensile load indicated on the y-axis and deflection on the x-axis. The graphs are allocated into two distinct regions: the elastic area and the plastic area. The amounts for tensile load and deflection for two mm and three mm width show variations; however, these variations are not significant. In both graphs, the elastic deformation region shows a undeviating relationship up to the onset of plastic deformation, which then proceeds in a nonlinear manner. The distinction between the regions of elastic and plastic deformation is not clearly apparent. The progression of plastic deformation continues to the apex of the curve until failure is reached. At the apex of the curve associated with the extreme load, there would be crack initiation may take place and advance with reducing load up to failure occurs.

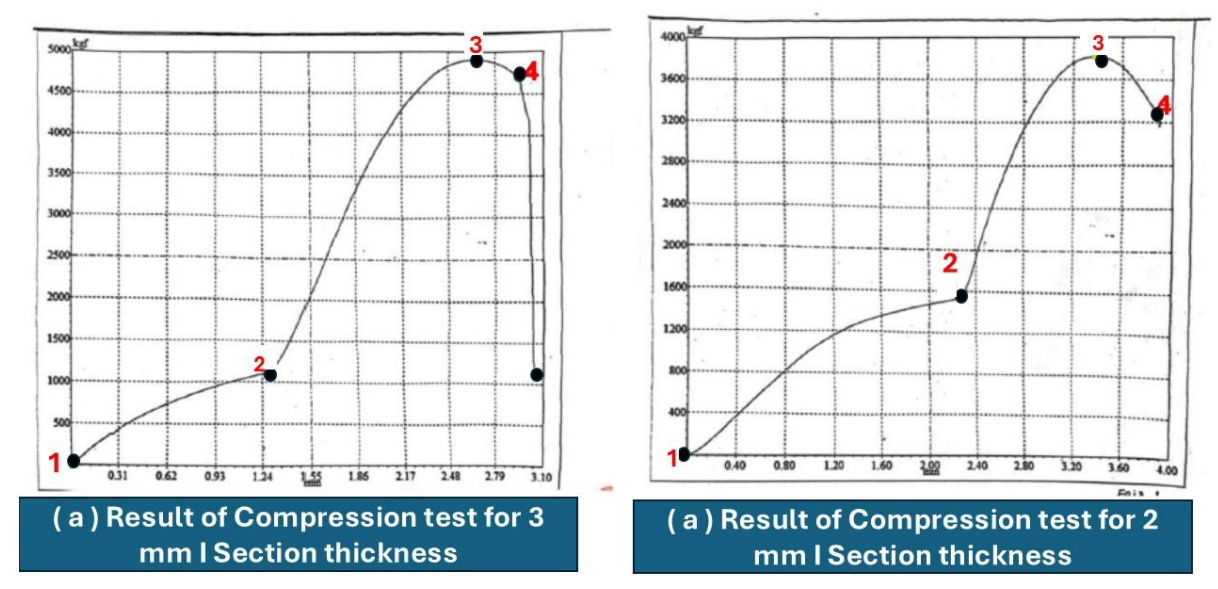


Figure 17 The I-section tensile test load-dflection diagram. 1-2 = elastic, 2-4 = plastic, 3 = maximum load. 4 = rupture.

The data shows a peak load of 4905 kg accompanied by a deflection of 2.68 mm for a width of 3 mm. The maximum tensile load with a 2 mm I-section width is 3820 N, resulting in a deflection of 3.35 mm. The 3 mm I-section width exhibits a 22% reduction in deflection and a 28% increase in tensile load compared to the 2 mm section. The rupture load for a 3 mm specimen is measured at 4651 N, accompanied by a deflection of 2.82 mm. I-sections with a width of 2 mm fail at a load of 3281 N, exhibiting a deflection of 3.83 mm. The deflection is reduced by 23.9%, while the breaking load for three mm is 41.9% greater than that of two mm. The data indicates that the maximum load limit of elasticity is 1110 N with a deflection of 1.23 mm for a three mm I-section, while for a two mm I-section, it is 1521 N with a deflection of 2.23 mm. The findings indicate that 2 mm I-sections exhibit greater ductility compared to their 3 mm counterparts. The 2 mm I-Section exhibits a greater yield point, whereas the 3 mm I-Section demonstrates a larger ultimate tensile load.

Among all connecting rods, only sample numbers I and II were found to be broken. The microstructure depicted in Figure 18 reveals the presence of carbide, as anticipated. The connecting rod exhibits brittleness and fractures under tensile testing because of carbide presence. Additional samples exhibit bending.

2025, 10(3) e-ISSN: 2468-4376

https://www.jisem-journal.com/

### **Research Article**

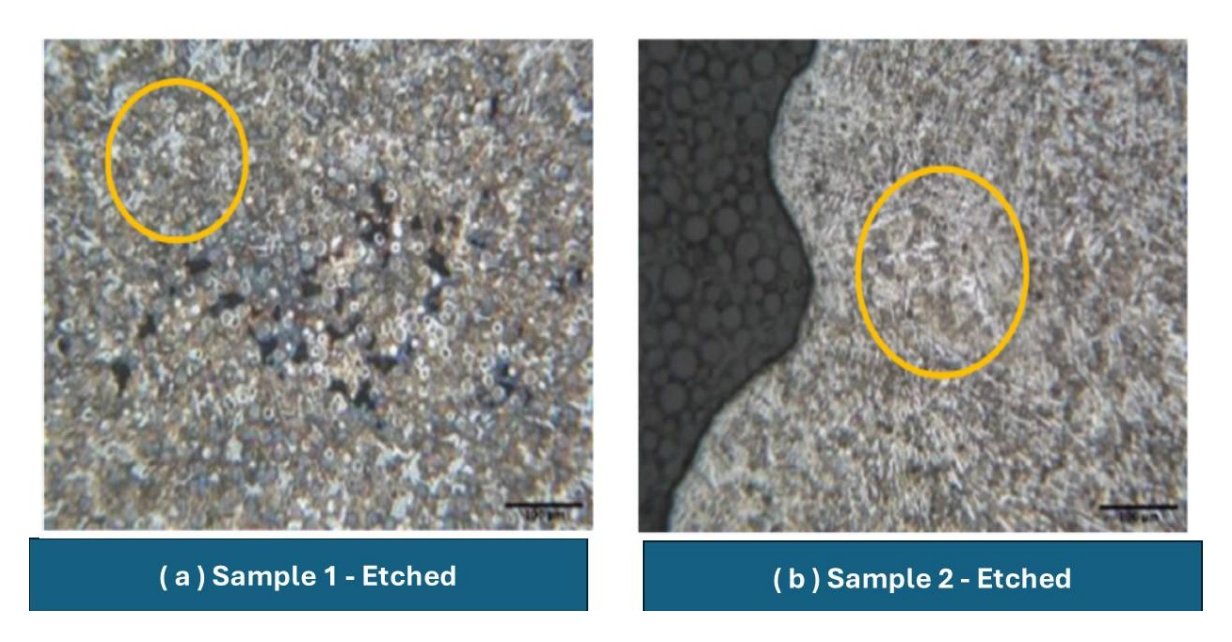


Figure 18 Microstructures of fractured samples one and two.

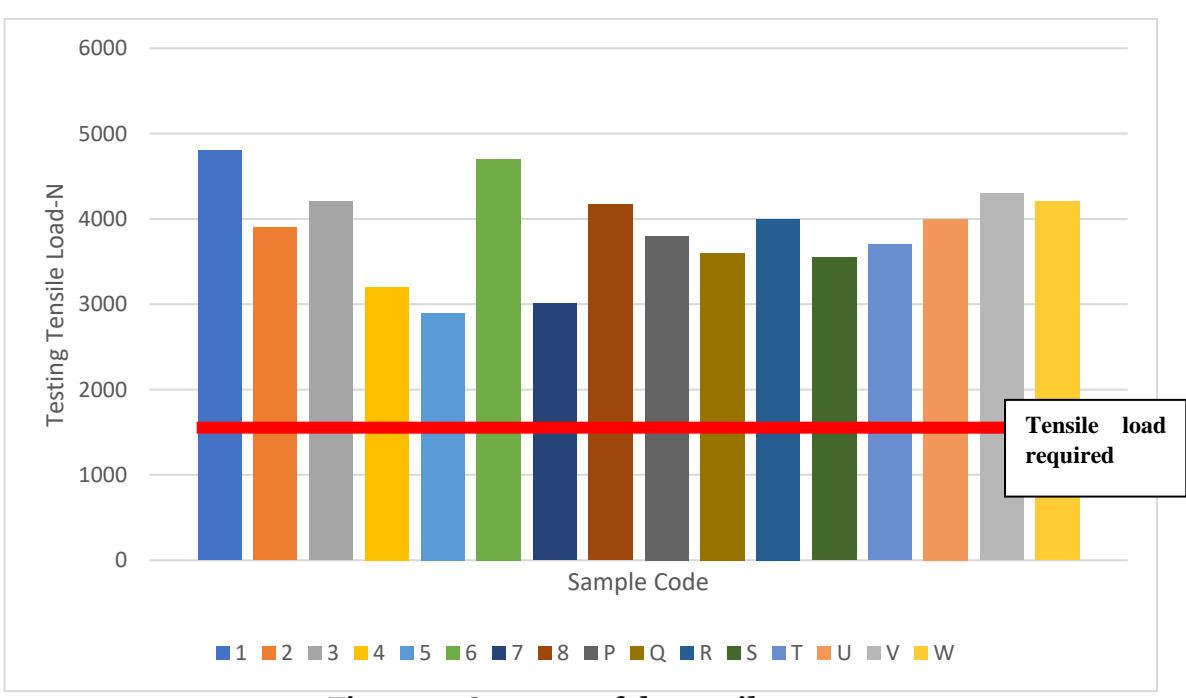


Figure 19 Outcome of the tensile test.

The tensile loads for each connecting rod are illustrated in Figure 19. The tensile loads all surpass the specified requirement of 1458 N. The connecting rod shows an average tensile load of 3959 N with a 3 mm I-section width, whereas the average load for a two mm I-section width is 3925 N. Observed variation in the average tensile load is 0.7%, a value that can be regarded as negligible. As a result, the tensile load is likely to stay stable. This result is consistent with the finding from our earlier study [26], which reported a value of 3523 N.

### Conclusion

The validation of the casting design for producing a connecting rod with a 1.5 mm I-section width has been successfully achieved. The 1.5 mm I-section connecting rod has been duplicated 6 times in this study,

2025, 10(3) e-ISSN: 2468-4376

https://www.jisem-journal.com/

### **Research Article**

consistently producing dependable results in both microstructure and tensile load tests. The connecting rod design, characterized by a 1.5 mm I section width, has been effectively replicated on two occasions, producing consistent results in each case. The lack of Ni, combined with an abundance of Cu, ambition result in a matrix primarily made up of pearlite or ferrite-pearlite. The etched microstructure has validated these conditions, primarily characterized by the presence of a carbide matrix. This investigation also revealed a non-uniform microstructure in the I-section and big end. The microstructure condition exhibits notable variation involving the I section and the big end of the majority of connecting rods.

The results concerning the tensile load for both 2 mm and 1.5 mm I beam width reveal that both connecting rods demonstrate similar tensile loads, surpassing the standards established by the original connecting rod.

### References

- 1. Oktaviano, Y., M. Fadhlan, and R.D. Sulamet-Ariobimo, *Kekutan lelah ductile iron thin wall connecting rod vespa px-150* POROS, 2023. **19**(1): p. 44-52.
- 2. Misch, F. and P. Wingender, Revisiting carbon leakage. Energy Economics, 2024. 10(2): p. 107-122.
- 3. Zhang, W. and J. Xu, Advanced lightweight materials for Automobiles: A review. Materials & Design, 2022. **221**: p. 110994.
- 4. Cecchel, S., *Materials and technologies for lightweighting of structural parts for automotive applications*. SAE International Journal of Materials and Manufacturing, 2021. **14**(1): p. 81-98.
- 5. Tubić Bulat, B., Z. Zovko Brodarac, and P. Mrvar. *Nucleation and graphite growth in nodular cast iron—an overeview.* in 19th INTERNATIONAL FOUNDRYMEN CONFERENCE Humans-Valuable Resource for Foundry Industry Development. 2021. University of Zagreb Faculty of Metallurgy.
- 6. Taoudi, A., et al., *Design and optimization of a mild hybrid electric vehicle with energy-efficient longitudinal control.* SAE International Journal of Electrified Vehicles, 2021. **10**(1): p. 55-78.
- 7. Tran, M.-K., et al., *Design of a hybrid electric vehicle powertrain for performance optimization considering various powertrain components and configurations.* Vehicles, 2020. **3**(1): p. 20-32.
- 8. Alcázar-García, D. and J.L.R. Martínez, *Model-based design validation and optimization of drive systems in electric, hybrid, plug-in hybrid and fuel cell vehicles.* Energy, 2022. **254**: p. 123719.
- 9. Mourad, M., S. El-Hadad, and M. Ibrahim, *Influence of inoculant type on the microstructure characteristics and mechanical properties of ductile iron*. Transactions of the Indian Institute of Metals, 2020. **73**: p. 1027-1041.
- 10. Riposan, I., et al., *Structure characteristics of high-Si ductile cast irons*. International Journal of Metalcasting, 2023. **17**(4): p. 2389-2412.
- 11. Lekakh, S.N., et al., *Control of high-temperature static and transient thermomechanical behavior of SiMo ductile iron by Al alloying.* International Journal of Metalcasting, 2023. **17**(1): p. 22-38.
- 12. Liu, C., et al., *Effects of graphite nodule count on mechanical properties and thermal conductivity of ductile iron*. Materials Today Communications, 2022. **31**: p. 103522.
- 13. Colin-García, E., et al., *Nodule count effect on microstructure and mechanical properties of hypo-eutectic ADI alloyed with nickel.* Journal of Mining and Metallurgy, Section B: Metallurgy, 2021. **57**(1): p. 115-124.
- 14. Schüssler, J. and A. Bührig-Polaczek, *Thermal analysis of ductile iron: a new way to predict the mechanical properties*. International Journal of Metalcasting, 2024: p. 1-14.
- 15. Hasanzadeh, R., et al., *Process-property relationship in polylactic acid composites reinforced by iron microparticles and 3D printed by fused filament fabrication*. Polymer Engineering & Science, 2024. **64**(1): p. 399-411.
- 16. Keskin, M.E., et al., *Investigation of The Effect of Molding Material Difference on Design in GGG70 Ductile Cast Iron Production*. Türk Doğa ve Fen Dergisi, 2024. **13**(2): p. 14-20.
- 17. Li, Z., et al., International Journal of Lightweight Materials and Manufacture.
- 18. Sulamet-Ariobimo, R.D., et al., *The effects of I-Beam thickness to microstructure and compression load of thin wall ductile iron connecting rod.* International Journal of Lightweight Materials and Manufacture, 2023. **6**(3): p. 392-404.
- 19. Keleş, A., R. Cengız, and M. Yildirim, Effect of Alloying Elements and Technological Parameters of Austempering on the Structure and Mechanical Properties of Ductile Cast Iron (ADI). Metal Science and Heat Treatment, 2023. **65**(3): p. 191-199.
- 20. Abdelrahim, D.M., E.E. Ateia, and A.A. Nofal, *Effect of molybdenum contents on microstructure and high-temperature wear behavior of SiMo ductile Iron*. International Journal of Metalcasting, 2024. **18**(1): p. 530-545.
- 21. Boulifa, I. and A. Hadji, *Study of the influence of alloying elements on the mechanical characteristics and wear behavior of a ductile cast iron*. Frattura ed Integrità Strutturale, 2021, **15**(56): p. 74-83.

2025, 10(3)

e-ISSN: 2468-4376

https://www.jisem-journal.com/

### **Research Article**

- 22.Ram, N. and V. Gautam, *Prediction of effect of alloying elements on properties of ferritic grade Si-Mo ductile cast iron using regression analysis.* Materials Today: Proceedings, 2022. **62**: p. 3855-3859.
- 23. Mathur, S. and S.R. Pulivarti, *Improvements in Productivity and Quality for Ductile Iron Flange Castings Using Simulation Technique*. Journal of Production and Industrial Engineering, 2022. **3**(2): p. 16-20.
- 24. Bauer, B., et al., *Influence of chemical composition and cooling rate on chunky graphite formation in thick-walled ductile iron castings*. International Journal of Metalcasting, 2023. **17**(3): p. 2050-2061.
- 25. Sulamet-Ariobimo, R.D., et al. *The application of thin wall ductile iron process in connecting rod.* in *AIP Conference Proceedings.* 2023. AIP Publishing.
- 26. Sulamet-Ariobimo, R., et al. *Effects of Austempering Process to Mechanical Properties of Thin Wall Ductile Iron Connecting Rod.* in *IOP Conference Series: Materials Science and Engineering*. 2019. IOP Publishing.